



HAL
open science

Col-OSSOS: Compositional Homogeneity of Three Kuiper Belt Binaries

Michael Marsset, Wesley Fraser, Michele Bannister, Megan Schwamb, Rosemary Pike, Susan Benecchi, J. Kavelaars, Mike Alexandersen, Ying-Tung Chen, Brett Gladman, et al.

► To cite this version:

Michael Marsset, Wesley Fraser, Michele Bannister, Megan Schwamb, Rosemary Pike, et al.. Col-OSSOS: Compositional Homogeneity of Three Kuiper Belt Binaries. *The Planetary Science Journal*, 2020, 1 (1), pp.16. 10.3847/PSJ/ab8cc0 . hal-02884321

HAL Id: hal-02884321

<https://hal.science/hal-02884321v1>

Submitted on 17 Dec 2020

HAL is a multi-disciplinary open access archive for the deposit and dissemination of scientific research documents, whether they are published or not. The documents may come from teaching and research institutions in France or abroad, or from public or private research centers.






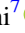







L'archive ouverte pluridisciplinaire **HAL**, est destinée au dépôt et à la diffusion de documents scientifiques de niveau recherche, publiés ou non, émanant des établissements d'enseignement et de recherche français ou étrangers, des laboratoires publics ou privés.



Distributed under a Creative Commons Attribution 4.0 International License



Col-OSSOS: Compositional Homogeneity of Three Kuiper Belt Binaries

Michaël Marsset^{1,2} , Wesley C. Fraser² , Michele T. Bannister³ , Megan E. Schwamb^{2,4} , Rosemary E Pike^{5,6} ,
Susan Benecchi⁷ , J. J. Kavelaars^{8,9} , Mike Alexandersen^{5,6} , Ying-Tung Chen⁵ , Brett J. Gladman¹⁰ ,
Stephen D. J. Gwyn⁸ , Jean-Marc Petit¹¹ , and Kathryn Volk¹² 

¹ Department of Earth, Atmospheric and Planetary Sciences, MIT, 77 Massachusetts Avenue, Cambridge, MA 02139, USA; michael.marsset@qub.ac.uk

² Astrophysics Research Centre, Queen's University Belfast, Belfast BT7 1NN, UK

³ School of Physical and Chemical Sciences—Te Kura Matū, University of Canterbury, Private Bag 4800, Christchurch 8140, New Zealand

⁴ Gemini Observatory, Northern Operations Center, 670 North A'ohoku Place, Hilo, HI 96720, USA

⁵ Institute of Astronomy and Astrophysics, Academia Sinica; 11F of AS/NTU Astronomy-Mathematics Building, No.1, Sec. 4, Roosevelt Rd Taipei 10617, Taiwan, R.O.C.

⁶ Harvard & Smithsonian Center for Astrophysics, 60 Garden Street, Cambridge, MA 02138, USA

⁷ Planetary Science Institute, 1700 East Fort Lowell, Suite 106, Tucson, AZ 85719, USA

⁸ NRC-Herzberg Astronomy and Astrophysics, National Research Council of Canada, 5071 West Saanich Road, Victoria, BC V9E 2E7, Canada

⁹ Department of Physics and Astronomy, University of Victoria, Elliott Building, 3800 Finnerty Road, Victoria, BC V8P 5C2, Canada

¹⁰ Department of Physics and Astronomy, University of British Columbia, Vancouver, BC V6T 1Z1, Canada

¹¹ Institut UTINAM UMR6213, CNRS, Univ. Bourgogne Franche-Comté, OSU Theta F-25000 Besançon, France

¹² Lunar and Planetary Laboratory, The University of Arizona, 1629 East University Boulevard, Tucson, AZ 85721, USA

Received 2020 January 22; revised 2020 April 20; accepted 2020 April 22; published 2020 May 20

Abstract

The surface characterization of Trans-Neptunian binaries (TNBs) is key to understanding the properties of the disk of planetesimals from which these objects formed. In the optical wavelengths, it has been demonstrated that most equal-sized component systems share similar colors, suggesting they have a similar composition. The color homogeneity of binary pairs contrasts with the overall diversity of colors in the Kuiper Belt, which was interpreted as evidence that Trans-Neptunian objects (TNOs) formed from a locally homogeneous and globally heterogeneous protoplanetary disk. In this paradigm, binary pairs must have formed early, before the dynamically hot TNOs were scattered out from their formation location. The latter inferences, however, relied on the assumption that the matching colors of the binary components imply matching composition. Here, we test this assumption by examining the component-resolved photometry of three TNBs found in the Outer Solar System Origins Survey: 505447 (2013 SQ99), 511551 (2014 UD225), and 506121 (2016 BP81), across the visible and J -band near-infrared wavelength range. We report similar colors within 2σ for the binary pairs, which is suggestive of similar reflectance spectra and hence surface composition. This advocates for gravitational collapse of pebble clouds as a possible TNO formation route. However, we stress that several similarly small TNOs, including at least one binary, have been shown to exhibit substantial spectral variability in the near-infrared, implying color equality of binary pairs is likely to be violated in some cases.

Unified Astronomy Thesaurus concepts: [Trans-Neptunian objects \(1705\)](#); [Broad band photometry \(184\)](#)

1. Introduction

Since the discovery of Pluto's moon Charon (Christy & Harrington 1978), more than a hundred binaries have been detected in the Kuiper Belt,¹³ the population of planetesimals near and beyond the orbit of Neptune. Several mechanisms have been invoked for the origin of these systems, from mutual gravitational captures (Goldreich et al. 2002; Funato et al. 2004; Schlichting & Sari 2008) to disruptions of fast rotators (Ortiz et al. 2012) and co-formation through gravitational collapses of pebble clouds in the primordial turbulent disk (Johansen et al. 2007; Nesvorný et al. 2010). Each formation mechanism is expected to result in different physical properties, such as size, size ratio, orbit pole orientation, and (dis)similarity in composition, of the Trans-Neptunian binaries'

(TNBs) components. Simulations of co-formation by gravitational collapses currently provide the best match to the observed properties of the equal-size TNBs (Nesvorný et al. 2019; Robinson et al. 2020), including their prevalence (Noll et al. 2008; Fraser et al. 2017; although maybe not at small sizes, $H_r > 7.5$; Pike et al. 2020), their broad inclination distribution, and their predominantly prograde orbits (Grundy et al. 2019). This scenario also explains the high fraction of widely separated binaries in the dynamically quiescent “cold” (low inclination and eccentricity) population of the Kuiper Belt, compared to the dynamically “hot” component where wide binaries would have been disrupted by Neptune scattering (Parker & Kavelaars 2010; Nesvorný & Vokrouhlický 2019). In this scenario, the TNBs would share the same composition, having accreted in the same environment.

In the optical wavelengths, Benecchi et al. (2009) found that the components of similar-sized TNBs share the same colors and interpreted this as evidence that they have similar composition. The similar colors of the pair members further contrast with the variety of colors among the overall population of Trans-Neptunian objects (TNOs; e.g., Tegler & Romanishin 1998, 2000, 2003; Tegler et al. 2003, 2008, 2016; also see

¹³ <http://www2.lowell.edu/users/grundy/tnbs/status.html> 106 binary systems as of 2020 April 20.



Peixinho et al. 2003, 2012, 2015; Fraser & Brown 2012; Lacerda et al. 2014; Fraser et al. 2015; Pike et al. 2017; Wong & Brown 2017; Alvarez-Candal et al. 2019; Marsset et al. 2019; Schwamb et al. 2019; Thirouin & Sheppard 2019), suggesting these objects formed from a locally homogeneous and globally heterogeneous protoplanetary disk. This inference, however, relies on the assumption that matching optical colors imply matching composition. However, optical colors are not sufficient to infer compositional (dis)similarities of the binary components, because different ices and chemical elements in the outer solar system share similar optical colors (e.g., Barucci et al. 2011), and many of these elements only distinctively reveal themselves outside of optical wavelengths. Measuring composition would normally require measuring albedo and reflectance spectra of the components across the full visible and near-infrared spectral ranges. As most TNOs are too faint for spectroscopy, one must instead rely on what near-simultaneous multiband photometry reveal as a proxy.

In this short paper, we present the colors of three TNBs across the visible and J -band wavelength range and test the assumption of an identical bulk composition for the primary and secondary components of each binary pair. To do so, we reanalyze recent near-simultaneous g -, r -, z -, and J -band photometric data collected with Gemini North through the Colors of the Outer Solar System Origins Survey (Col-OSSOS; Schwamb et al. 2019), in order to search for new TNBs and explore the spectral (dis)similarities of their components across these spectral bands.

2. Search and Characterization of Candidate Binaries

2.1. Observations

Photometric measurements presented in this paper were collected from the ground through Col-OSSOS (PI: W. Fraser) on the 8.1 m Frederick C. Gillett Gemini North Telescope on Maunakea. Col-OSSOS acquires near-simultaneous g , r , and J —and, for a subsample of objects, z (Pike et al. 2017)—photometry of a magnitude-limited subset of the OSSOS (Bannister et al. 2016, 2018) sample with $r < 23.6$ (Schwamb et al. 2019). Measurements were acquired in a $rg(z)J(z)gr$ sequence to monitor any light-curve effect, using the Gemini Multi-Object Spectrograph (GMOS; Hook et al. 2004) for measurements in the optical wavelengths and the Near InfraRed Imager and Spectrometer (NIRI; Hodapp et al. 2003) for those in the J band. Targets were tracked sidereally, meaning that stars appear pointlike on the images while the TNO is elongated in the direction of its projected motion on the sky. Exposures were limited to 300 s in the optical and 120 s in the J band in order to minimize trailing losses and to mitigate the sky background. The telescope was dithered between consecutive exposures in the same filter to account for pixel-to-pixel sensitivity variations. Observing circumstances for our targets can be found in Pike et al. (2017) and Schwamb et al. (2019).

2.2. Data Reduction

The data reduction and photometric extraction of the Gemini data were performed as described in Schwamb et al. (2019). Here, we summarize the main steps. Processing of the GMOS data was achieved with the Gemini IRAF package. We first used the bias images acquired as part of the GMOS calibration plan to remove the bias offset from the science frames. Master

sky flats were produced from an average of the science frames with sources masked and were used to flatten these frames. Finally, the GMOS charge-coupled device (CCD) chips were mosaicked into a single extension.

For the NIRI images, flat-fielding was performed with a master flat built from the Gemini facility calibration unit flats. We produced one sky frame for each individual science image from a rolling average of the 15 temporally closest science images with sources masked, in order to account for temporal sky variation. Images acquired at similar dither positions to the image to sky-subtract were not used to compute the average sky frame. Bad pixel maps were created from the individual dark exposures, using the longest exposures to flag dead and low-sensitive pixels, and the shortest ones to identify hot pixels. These maps were then combined with the NIRI static bad pixel map provided in the Gemini IRAF package. Individual sky-subtracted images were aligned sidereally using multiple star centroids in order to create a deep stacked image of pointlike stars that can be used to compute the mean point-spread function (PSF) of the image. A second stack was produced shifting the frames at the TNO’s on-sky velocity derived from the Minor Planet Center (MPC) Minor Planet and Comet Ephemeris Service.¹⁴ Finally, cosmic-ray rejection was performed on the stacked images using the Python implementation of the L.A.Cosmic (Laplacian Cosmic Ray Identification) algorithm.¹⁵

2.3. Trailed PSF Fitting

A binary search was performed using the complete set of GMOS and NIRI images acquired for each target in the Col-OSSOS survey. We calculated and subtracted the trailed PSF (TSF) of each image with the TRIPPY software package (Fraser et al. 2016). The TSF is the equivalent of the PSF for a moving object. The details of the method used to model the TSF are provided in Fraser et al. (2016). We describe it briefly here. First, the PSF of each GMOS image and the NIRI stack of images was measured by fitting a Moffat profile to each stellar (pointlike) source on the frame. The best-fit solution was derived by finding the minimum χ^2 residual between the mean stellar profile and the modeled Moffat profile. Next, the mean Moffat profile was subtracted from each stellar source to create a mean residual image, which was then added to the mean Moffat profile. The resulting Moffat+residual profile was convolved with a line that has the length and angle that best describes the known on-image rate of motion of the TNO to produce the TSF. The TSF was then fitted to the TNO image using the emcee Python implementation of Foreman-Mackey et al. (2013, 2019)’s Markov Chain Monte Carlo (MCMC) ensemble sampler. A total of 20 walkers with three free parameters, the (x, y) positions and flux of the TNO, were used to find the minimum χ^2 residual between the model and the image. Once a solution was found, uncertainties on the parameters were calculated as the 1σ deviation of the walkers across an extra 100 iteration steps. Finally, we built stacks of the residual images acquired in the same filter for each object in our data set in order to increase the signal-to-noise ratio of the residual and to search for very faint companions.

¹⁴ <http://www.minorplanetcenter.net/iau/MPEph/MPEph.html>. Orbits, and thus on-sky velocities, are those published in Bannister et al. (2018).

¹⁵ <http://www.astro.yale.edu/dokkum/lacosmic/>

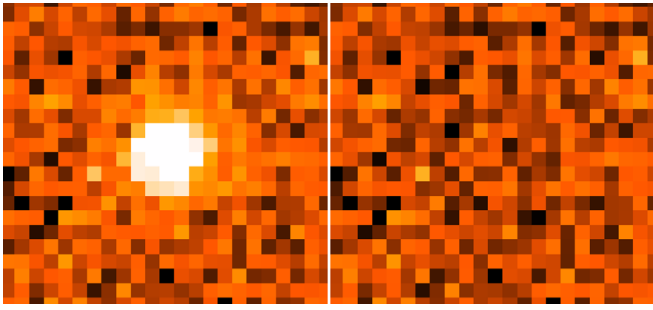


Figure 1. Example of single-TSF subtraction of a non-binary TNO with the TRIPPy software (Fraser et al. 2016). Left: original NIRI stacked image of 500836 (2013 GQ137; OSSOS ID o3e21). Right: single-TSF subtracted image. The residuals are indistinguishable from the background noise. Image scales, contrast, and color bars are the same for the two images.

2.4. Analysis of the Residuals

Three distinct kinds of residuals are revealed by our analysis. The first kind is consistent with the TNO being a single source. In that case, the residuals are indistinguishable from the background noise, i.e., the pixel values in the region of the subtracted TNO follow a Poisson distribution (Figure 1). In the case of a double source, two categories of residuals are observed. When the binary has roughly similar-sized components, a “butterfly” pattern is revealed as a result of subtracting a single TSF from a double-peak signal. When the brightness contrast between the two components is large, the primary is efficiently fitted and removed by the TSF, and a round, secondary source is revealed in the residuals. Double-TSF fitting on these double sources result in residuals that are indistinguishable from the background.

Our analysis allowed the identification of three TNBs among 75 objects searched in the Col-OSSOS data set: 511551 (2014 UD225), 506121 (2016 BP81), and 505447 (2013 SQ99). Images of the binaries are shown in Figure 2¹⁶ and their parameters and observing circumstances are provided in Table 1. All three objects come from the first (2014B) semester of Col-OSSOS observations and their discovery has been previously reported by Fraser et al. (2017). No other TNB could be identified in the subsequent Col-OSSOS semesters. We attribute this to the worse seeing conditions experienced during later semesters with respect to our first semester of observations, where seeing was between $0''.4$ and $0''.5$.

In the case of 511551, the components’s brightness ratio is large and single-TSF fitting efficiently removed the primary and revealed the presence of a smaller companion. In the case of 506121 and 505447, the components have roughly similar brightness, and TSF subtraction produced a “butterfly shaped” residual (Figure 2). The physical properties—angular separation and components’s brightness ratio—of the three binaries are investigated in the following section.

2.5. Component-resolved Photometry

The angular separation and components’s brightness ratio of the binaries were derived through double-TSF fitting using TRIPPy. We began by estimating the center position and

¹⁶ From top to bottom, those correspond to the r -band image `mrgN20140826S0221.fits` of 511551 (2014 UD225), the r -band image `mrgN20140826S0174.fits` of 506121 (2016 BP81), and the g -band image `mrgN20140822S0267.fits` of 505447 (2013 SQ99; file names listed in the Gemini Observatory Archive).

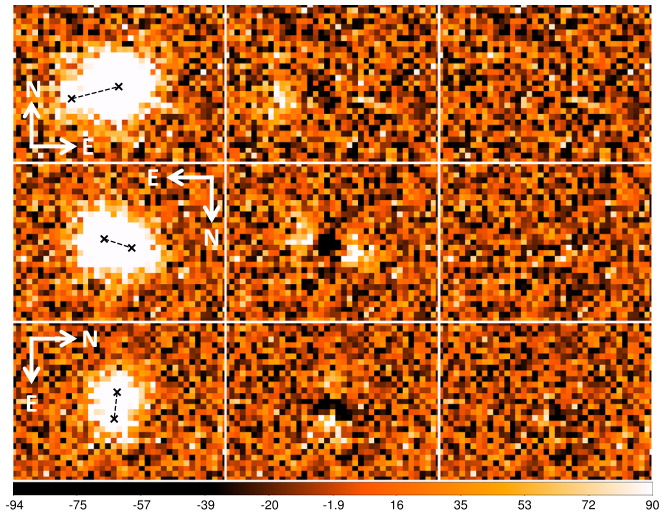


Figure 2. Left column: GMOS images acquired on Gemini North for 511551 (2014 UD225; top), 506121 (2016 BP81; middle), and 505447 (2013 SQ99; bottom). Black crosses indicate the location of the two components’s centroids as determined by the TSF fitting procedure. The white arrows indicate the equatorial north (N) and east (E) directions. Middle column: single-TSF subtraction reveals the binarity of the three TNOs. Right column: double-TSF subtraction efficiently removes the two binary components, with a residual consistent with the background. Image scale, contrast, and color bar are the same for all images.

brightness ratio of the two binary components by eye using both the original images and the single-TSF subtracted ones. The best-fit solution was then derived for each observation through automated MCMC fitting of the sky-subtracted image. We used a total of 30 walkers, each performing a total number of a few hundred steps in the six-parameter space defined by the position and flux of the primary (x_1 , y_1 , and f_1) and secondary (x_2 , y_2 , and f_2) components of the binary. At each step, a standard χ^2 formula was used to evaluate the goodness of the fit between the synthetic double-TSF image and the science image, using an uncertainty map to mitigate the influence of bad pixels when evaluating the χ^2 . Once the walkers converged toward a stable solution, an additional 100 steps per walker were run and recorded. We adopted x_1 , y_1 , f_1 , x_2 , y_2 , and f_2 as best-fit parameters to the median value of these parameters across the 30×100 steps, and the uncertainty as their 1σ deviation with respect to the median value. Results of our MCMC fitting analysis for individual images are reported in Table 2. Adopted physical properties of the binaries—including their component separation and brightness ratio—are provided in Table 3.

Next, we computed the component-resolved colors of the binaries by combining their measured f_2/f_1 component brightness ratio with the magnitudes of the binaries converted to the Sloan Digital Sky Survey (SDSS) photometric system reported in Schwamb et al. (2019). In each image, f_2/f_1 was calculated directly from the amplitude coefficients used to scale the TRIPPy TSFs to match image brightnesses. Fluxes were estimated from planted sources in blank images, and from both, mean colors were measured in $(g-r)$, $(r-z)$, and $(r-J)$. Quoted uncertainties include the brightness ratio ranges from the fits, the Poisson statistics uncertainties, the zero-point uncertainties, the background uncertainties, and the aperture correction uncertainties. The derived $(g-r)$, $(r-z)$, and $(r-J)$ colors of the binaries and their associated uncertainties

Table 1
Orbital Parameters and Observing Circumstances for the Three Binaries

Target Number	MPC Designation	OSSOS ID	a (au)	e	inc ($^\circ$)	Orbital Classification	Mean m_r (SDSS)	H_r	Δ (au)	r_H (au)	α ($^\circ$)	Average Air Mass	Mean MJD
511551	2014 UD225	o4h45	43.36	0.130	3.66	Cold classical	22.98 ± 0.05	6.55	43.68	44.29	1.05	1.03	56 895.554 093
"	"	"	"	"	"	"	23.17 ± 0.04	"	43.65	"	1.02	1.38	56 897.438 239
506121	2016 BP81	o3l39	43.68	0.076	4.18	7:4 Resonator	22.83 ± 0.11	6.58	41.81	42.54	0.96	1.13	56 895.471 738
505447	2013 SQ99	o3l76	44.15	0.093	3.47	Cold classical	23.17 ± 0.04	6.45	46.60	47.34	0.85	1.05	56 891.544 967

Note. Geometric parameters and derived H_r are reported for the time of the Col-OSSOS observation: r_H : heliocentric range, Δ : observer range, and α : phase angle. Orbital classifications are from Bannister et al. (2018). 511551 (2014 UD225) was observed at two distinct epochs in Col-OSSOS. Only one image from the second epoch shows evidence of binarity and was used in our analysis.

Table 2
Results of Double-TSF Fitting

Object	Image	Filter	MJD	FWHM (")	Separation (")			Brightness Ratio ^b ($\frac{f_2}{f_1}$)
					δ R.A. cos(decl.) ^a	δ decl. ^a	Distance	
505447	N20140822S0260.fits	z_G0304	56 891.505 249 5	0.42	-0.41 ± 0.02	0.06 ± 0.02	0.41 ± 0.02	$0.65^{+0.13}_{-0.09}$
"	N20140822S0261.fits	z_G0304	56 891.509 676 1	0.33	$-0.38^{+0.02}_{-0.01}$	0.04 ± 0.02	0.38 ± 0.01	$0.54^{+0.06}_{-0.07}$
"	N20140822S0262.fits	z_G0304	56 891.514 097 9	0.36	-0.37 ± 0.01	$0.02^{+0.02}_{-0.01}$	$0.37^{+0.01}_{-0.02}$	$0.61^{+0.06}_{-0.05}$
"	N20140822S0263.fits	z_G0304	56 891.518 519 5	0.36	-0.37 ± 0.02	$0.02^{+0.01}_{-0.02}$	0.37 ± 0.02	$0.60^{+0.05}_{-0.04}$
"	N20140822S0264.fits	r_G0303	56 891.522 989 9	0.39	-0.37 ± 0.01	0.02 ± 0.01	0.37 ± 0.01	0.71 ± 0.06
"	N20140822S0265.fits	g_G0301	56 891.527 493 9	0.41	-0.38 ± 0.01	$0.03^{+0.01}_{-0.02}$	0.38 ± 0.01	$0.80^{+0.06}_{-0.08}$
"	N20140822S0266.fits	g_G0301	56 891.531 922 0	0.41	-0.38 ± 0.01	0.03 ± 0.02	0.38 ± 0.01	$0.59^{+0.06}_{-0.05}$
"	N20140822S0267.fits	g_G0301	56 891.536 366 1	0.45	-0.34 ± 0.02	0.04 ± 0.02	0.35 ± 0.02	$0.70^{+0.10}_{-0.12}$
"	O13BL3TF.fits	J	56 891.586 420 4	0.44	$-0.37^{+0.03}_{-0.02}$	0.02 ± 0.02	$0.38^{+0.03}_{-0.02}$	$0.66^{+0.08}_{-0.06}$
511551	N20140826S0184.fits	r_G0303	56 895.531 939 2	0.49	$0.66^{+0.04}_{-0.05}$	$0.12^{+0.06}_{-0.04}$	0.69 ± 0.04	0.11 ± 0.02
"	N20140826S0185.fits	g_G0301	56 895.536 441 6	0.54	0.72 ± 0.05	0.30 ± 0.04	$0.80^{+0.04}_{-0.05}$	0.12 ± 0.02
"	N20140826S0217.fits	g_G0301	56 895.600 471 2	0.53	$0.65^{+0.03}_{-0.04}$	$0.15^{+0.03}_{-0.04}$	$0.69^{+0.03}_{-0.04}$	$0.14^{+0.02}_{-0.01}$
"	N20140826S0218.fits	g_G0301	56 895.604 895 8	0.52	$0.67^{+0.03}_{-0.04}$	0.16 ± 0.03	$0.71^{+0.03}_{-0.04}$	0.14 ± 0.01
"	N20140826S0219.fits	g_G0301	56 895.609 328 9	0.53	0.71 ± 0.03	0.16 ± 0.02	0.75 ± 0.03	0.15 ± 0.01
"	N20140826S0220.fits	r_G0303	56 895.613 824 0	0.53	$0.64^{+0.03}_{-0.02}$	0.14 ± 0.02	$0.67^{+0.03}_{-0.02}$	0.14 ± 0.01
"	N20140826S0221.fits	r_G0303	56 895.618 251 1	0.53	0.58 ± 0.02	$0.16^{+0.01}_{-0.02}$	0.62 ± 0.02	0.18 ± 0.01
"	Col3N03.fits	J	56 895.576 247 2	0.55	0.61 ± 0.03	0.10 ± 0.04	0.64 ± 0.03	0.14 ± 0.02
"	N20140828S0128.fits	r_G0303	56 897.438 239 4	0.50	0.64 ± 0.04	$0.12^{+0.02}_{-0.03}$	0.65 ± 0.04	0.14 ± 0.02
506121	O13BL3RB.fits	J	56 895.456 420 7	0.62	0.43 ± 0.03	-0.11 ± 0.02	0.44 ± 0.04	$0.79^{+0.06}_{-0.08}$
"	N20140826S0173.fits	g_G0301	56 895.483 717 7	0.59	0.34 ± 0.02	$-0.15^{+0.01}_{-0.02}$	0.37 ± 0.02	$0.85^{+0.09}_{-0.15}$
"	N20140826S0174.fits	r_G0303	56 895.487 056 2	0.50	0.36 ± 0.01	-0.11 ± 0.01	0.38 ± 0.01	$0.77^{+0.07}_{-0.06}$

Notes.

^a Measured position of the brightest component minus position of the faintest one.

^b Measured flux of the faintest component divided by the measured flux of the brightest one.

Table 3
Mean Physical Properties of the Binaries

Object	Filter	Number of Images	Separation (")	Separation (10^3 km)	Brightness Ratio ($\frac{f_2}{f_1}$)
"	r_G0303	1	0.37 ± 0.01	12.7 ± 0.3	0.71 ± 0.06
"	z_G0304	4	0.38 ± 0.02	12.9 ± 0.7	$0.60^{+0.08}_{-0.06}$
"	J	1	$0.38^{+0.03}_{-0.02}$	$12.9^{+1.0}_{-0.7}$	$0.66^{+0.08}_{-0.06}$
511551	g_G0301	4	$0.74^{+0.03}_{-0.04}$	$23.5^{+1.0}_{-1.3}$	$0.14^{+0.02}_{-0.01}$
"	r_G0303	4	0.66 ± 0.03	21.0 ± 1.0	0.14 ± 0.01
"	J	1	0.64 ± 0.03	20.4 ± 0.6	0.14 ± 0.02
506121	g_G0301	1	0.37 ± 0.02	11.2 ± 0.6	$0.85^{+0.09}_{-0.15}$
"	r_G0303	1	0.37 ± 0.01	11.2 ± 0.3	$0.77^{+0.07}_{-0.06}$
"	J	1	0.44 ± 0.04	13.1 ± 1.2	$0.79^{+0.06}_{-0.08}$

are reported in Table 4 and are compared to the population of singletons in Figure 3.

Next, all color measurements were converted to a spectral slope (s), defined as the percentage increase in reflectance per 10^3 Å change in wavelength normalized to 550 nm, using the Synphot tool in the STSDAS software package¹⁷ (Lim et al. 2015). Specifically, this was achieved by forward modeling a Solar spectrum convolved with a set of linear spectra, with the spectral slope varying from neutral (0%/(10^3 Å)) to very red (50%/(10^3 Å)) with steps of 0.1%/(10^3 Å). We used the solar reference spectrum provided by the Hubble Space Telescope as part of the Synphot supplementary files. The array of models was then passed through Synphot to estimate the corresponding

colors in the various combinations of filters relevant for this work.

The derived spectral slope values are provided in Table 5. In the left panel of Figure 4, we plot the spectral slope of the primary component versus that of the secondary in the optical wavelength range, derived from (g-r) and (r-z) colors. Spectral slope values computed from (V-I) color measurements in Benecchi et al. (2009) are shown for comparison (here, the spectral slopes values were pulled directly from their paper). While these different colors do not probe the exact same wavelength range, the fact that the vast majority of TNOs exhibit linear spectral slopes in optical wavelengths makes it reasonable to compare these data sets. The right panel of Figure 4 shows a similar plot in the short near-infrared, derived from (r-J) color measurements. Because most TNOs show a

¹⁷ www.stsci.edu/institute/software_hardware/stsdas

Table 4
Colors of the Binaries

Object	Color Class ^a	H_r ^a	$(g - r)$			$(r - z)$			$(r - J)$		
			Binary ^a	Primary	Secondary	Binary ^a	Primary	Secondary	Binary ^a	Primary	Secondary
505447	red	6.45	0.98 ± 0.03	0.97 ± 0.07	$0.99^{+0.09}_{-0.11}$	0.56 ± 0.03	0.63 ± 0.07	0.45 ± 0.10	1.51 ± 0.06	$1.54^{+0.08}_{-0.09}$	$1.46^{+0.10}_{-0.11}$
511551	neutral	6.55	0.74 ± 0.02	0.74 ± 0.03	0.74 ± 0.13	1.42 ± 0.06	1.42 ± 0.06	$1.42^{+0.18}_{-0.16}$
506121	neutral	6.58	0.59 ± 0.03	$0.64^{+0.08}_{-0.10}$	$0.53^{+0.09}_{-0.14}$	1.60 ± 0.07	$1.59^{+0.10}_{-0.09}$	$1.62^{+0.11}_{-0.10}$

Note. For comparison, solar colors are $(g - r) = 0.45$, $(r - z) = 0.09$, and $(r - J) = 0.98$.

^a Schwamb et al. (2019).

Table 5
Spectral Gradients between Two Wavelengths

TNO Number	475–622 nm		622–905 nm		622–1250 nm	
	Primary	Secondary	Primary	Secondary	Primary	Secondary
505447	$32.5^{+4.1}_{-4.4}$	$34.1^{+5.2}_{-6.3}$	$28.1^{+5.4}_{-5.3}$	$15.5^{+6.2}_{-5.3}$	$12.0^{+2.6}_{-2.4}$	$9.7^{+3.0}_{-2.6}$
511551	$18.4^{+1.7}_{-1.7}$	$18.2^{+8.0}_{-8.2}$	$8.7^{+1.7}_{-1.6}$	$8.5^{+5.0}_{-3.7}$
506121	$12.2^{+4.8}_{-6.7}$	$4.7^{+5.8}_{-9.0}$	$13.4^{+3.3}_{-2.7}$	$14.3^{+4.0}_{-3.1}$

Note. Spectral gradients are in units of $\%/(10^3 \text{ \AA})$ and relative to 550 nm. A spectral slope of 0 corresponds to solar colors.

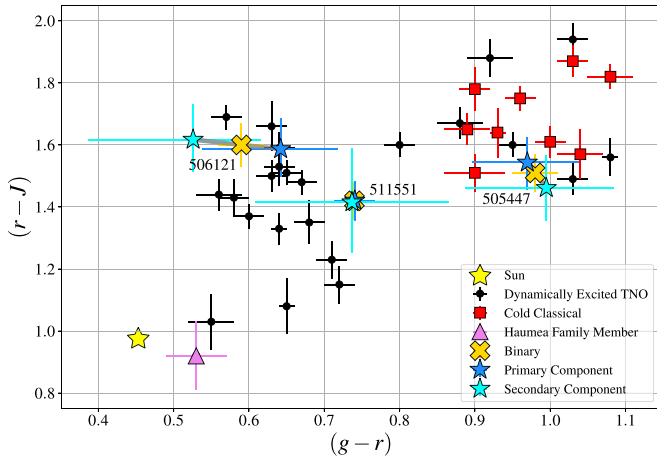


Figure 3. $(r - J)$ vs. $(g - r)$ color-color plot of the Col-OSSOS data set from Schwamb et al. (2019). The three binaries are marked by yellow crosses and their individual components by blue (primary component) and cyan (secondary component) stars. The International Astronomical Union number of each binary is indicated next to the corresponding data point. Measurements of two pair members belonging to the same system are linked by a gray line. Colors of the 511551 (2014 UD225) system and its components are almost equal, making them hard to distinguish in the figure. Other objects from the Col-OSSOS data set include singletons located on dynamically excited orbits (black dots) and classical objects with $i < 5^\circ$ (red squares). The object 2013 UQ15 (magenta triangle) is bluer than the Sun in $(r - J)$ and is dynamically consistent with the Haumea family. The solar color, with $(g - r) = 0.45$ and $(r - J) = 0.98$, is shown with the yellow star.

spectral inflexion close to $1 \mu\text{m}$, these measurements are shown in a different panel from the visible data. In both wavelength ranges, none of the three binaries deviates at the $>2\sigma$ level from the color correlation observed by Benecchi et al. (2009) in the optical, implying that the binary pairs most likely share similar optical and short near-infrared colors and, therefore, similar reflectance spectra and surface composition.

The largest color difference between two binary components in our sample is observed for 505447 (2013 SQ99) and is $\Delta(r - z) = 0.18$. 505447 is a very red object that belongs to the dynamically quiescent population of cold classical objects (Tegler & Romanishin 2000; Brown 2001). Compared to the g and r photometric bands, the z band was shown to probe a distinct spectral feature that is diagnostic of cold classical surfaces (Pike et al. 2017). Testing the correlation of colors in the $(r - z)$ wavelength range would be another useful test of surface homogeneity. Here, the observed $(r - z)$ color difference between the components of 505447 is an inconclusive 2σ result. For comparison, the largest color difference in $(g - r)$ color is found for 506121 (2016 BP81), $\Delta(g - r) = 0.11$, and is contained within the 1σ error bars on the measurements.

Compared to the other two binaries in our data set, 511551 (2014 UD225) exhibits a rather large brightness ratio of its components. Specifically, assuming the two components have a similar albedo, the primary would be about seven times more massive than the secondary. The similar colors of the components measured in this system suggests that the color homogeneity of TNO binaries remains valid for systems with such large mass ratios.

3. Discussion

The correlated colors of the TNB pairs across the full optical and near-infrared (J -band) spectral range advocates for similar reflectance spectra and hence surface compositions for these objects. While most TNO binaries studied so far are composed of equal mass components, this feature appears to remain valid for systems with rather large mass ratios, such as 511551 (2014 UD225), where the primary is about seven times more massive than the secondary (assuming they have a similar albedo). Considering the hypothesis that TNO surfaces are primordial and indicative of their formation location (Marsset et al. 2019), the surface equality of the binary pairs supports the two key assertions made by Benecchi et al. (2009) about TNO formation and the early outer solar system—namely, TNOs formed in a locally homogeneous and globally heterogeneous protoplanetary disk, and the formation of binaries must have happened early, before the violent dispersal of the disk that was driven by the migration of the gas giants, in order to explain the similar composition of their components. Taken together with other observed characteristics of the Kuiper Belt binaries—namely, (1) their nearly equal mass components ($m_2/m_1 > 10\%$; Noll et al. 2008), (2) their relatively wide mutual orbits (Parker & Kavelaars 2010), (3) their almost unanimous prograde orbital distribution (with the exception of the widest systems; Grundy et al. 2019), and (4) their predominance in the TNO population (Fraser et al. 2017)—this finding provides further support to the hypothesis of binary formation through the early gravitational collapse of pebble clouds in the turbulent gas disk (Nesvorný et al. 2010). Only this scenario is currently able to account simultaneously for all of the abovementioned properties of the TNO binary population. The predominance of binaries in the Kuiper Belt was recently reinforced by the New Horizons flyby imagery of (486958) Arrokoth (2014 MU69; Stern et al. 2019). This clearly showed Arrokoth to be a contact binary, implying a high binary fraction for systems below the current telescopic limits, at least in the cold classical population.

It should be noted, however, that several small TNOs are known to exhibit substantial color variability in the near-infrared that could relate to surface inhomogeneities induced by large impacts. This is the case, for instance, for the binary 26308

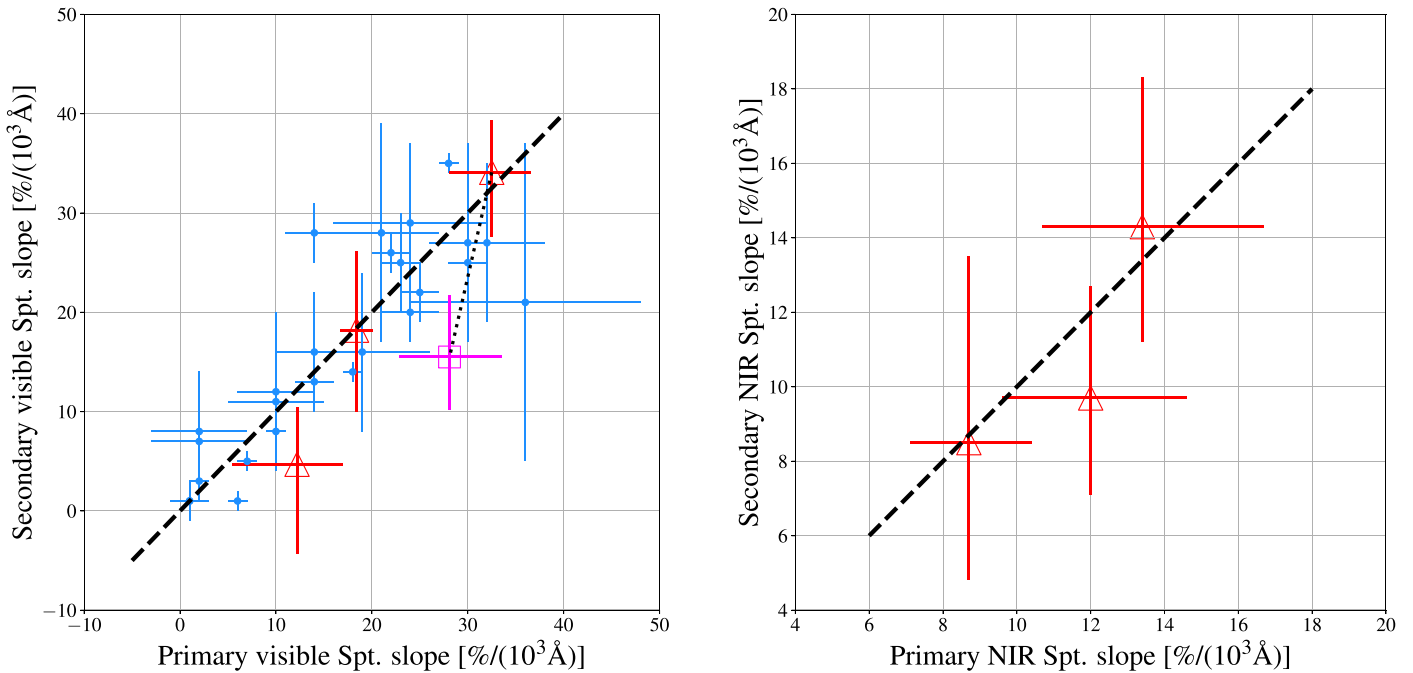


Figure 4. Left: secondary vs. primary optical spectral slopes of TNBs. The blue circles correspond to previous $(V - I)$ color measurements from Benecchi et al. (2009), and the red triangles and magenta square correspond to new measurements derived from our $(g - r)$ and $(r - z)$ colors, respectively. Spectral slope values for 505447 (2013 SQ99) derived from $(g - r)$ and $(r - z)$ colors are shown connected with a dotted line. Right: secondary vs. primary near-infrared (622–1250 nm) spectral slopes from this work. In both panels, the dashed line indicates a 1:1 ratio, corresponding to perfect color equality of the binary components. None of the three binaries deviate from the color correlation in the optical and short near-infrared at the 2σ level, supporting similar spectra and surface composition of their components.

(1998 SM165) that exhibits 0.2 mag variability in the J – K spectral region (Fraser et al. 2015). Two non-binary TNOs in the Col-OSSOS sample, 505448 (2013 SA100) and 2013 UN15, were also found to be spectrally variable in the optical and J band (Pike et al. 2017; Schwamb et al. 2019). Unless both components of such a system are rotationally locked and exhibit the same longitudinal color distributions, these highly spectrally variable systems must eventually break the color equality observed thus far. The reason why some systems were not found to have differently colored components over a large range of sizes ($H_V = 4.0$ – 8.1 in Benecchi et al. 2009) is likely due to the low spectral variability of TNOs in the optical (Fraser et al. 2015) with respect to the precision of the observations. It appears more likely that such a signal has merely been hidden, though we note that a few systems presented by Benecchi et al. (2009) exhibit 3σ deviations in the color difference of the primary and secondary.

Like the sample in Benecchi et al. (2009), none of the three binaries analyzed in this work are known to be spectrally variable in the optical and near-infrared (Schwamb et al. 2019). Although photometric sequences were acquired at a single epoch for each binary, their 1.7–3.0 hr duration allowed us to investigate spectral variability but returned no hint of spectral variability. Moreover, the precision of measurements achieved in this work is insufficient to detect a 0.2 mag near-infrared color variation of the components. The required photometric precision needed to detect such variability will, however, certainly be achievable by future large ground-based facilities equipped with adaptive optics (e.g., the Extremely Large Telescope; Gilmozzi & Spyromilio 2007; the Thirty Meter Telescope; Sanders 2013) and large space-based observatories (e.g., the James-Webb Space Telescope; Gardner et al. 2006). Future surveys of the Kuiper Belt will observe a small fraction of binary pairs with mismatched near-infrared colors.

4. Conclusion

We report component-resolved photometry for three TNBs across the visible and near-infrared spectral range. These three objects present evidence that their components have similar colors in the visible and the near-infrared, which is in agreement with Benecchi et al. (2009)’s finding that the components of a given TNB always share the same optical colors. This finding supports the inferences proposed by Benecchi et al. (2009) that TNB pairs share the same surface composition, thereby advocating for early binary formation in a locally homogeneous, globally heterogeneous protoplanetary disk. However, considering that several small TNBs are known to exhibit substantial color variability in the near-infrared, we anticipate that the color equality of the binary will break down in some cases as future surveys increase the known binary sample.














The authors acknowledge the sacred nature of Maunakea and appreciate the opportunity to observe from the mountain. This work is based on observations from the Large and Long Program GN-LP-1 (2014B through 2016B), obtained at the Gemini Observatory, which is operated by the Association of Universities for Research in Astronomy, Inc., under a cooperative agreement with the NSF on behalf of the Gemini partnership: the National Science Foundation (United States), the National Research Council (Canada), CONICYT (Chile), Ministerio de Ciencia, Tecnología e Innovación Productiva (Argentina), and Ministério da Ciência, Tecnologia e Inovação (Brazil). We thank the staff at Gemini North for their dedicated support of the Col-OSSOS program. Data was processed using the Gemini IRAF package. STSDAS and PyRAF are products of the Space Telescope Science Institute, which is operated by AURA for NASA. This research used the facilities of the

Canadian Astronomy Data Centre operated by the National Research Council of Canada with the support of the Canadian Space Agency. M.M. was supported by the National Aeronautics and Space Administration under grant No. 80NSSC18K0849 issued through the Planetary Astronomy Program. B.J.G. and J.J.K. acknowledge funding from NSERC Canada. J.-M.P. acknowledges funding from PNP-INSU, France. K.V. acknowledges funding from NASA (grants NNX15AH59G and 80NSSC19K0785).

Facilities: Gemini:Gillett (GMOSN, NIRI), CFHT (MegaCam).

Software: Astropy (Astropy Collaboration et al. 2013), Matplotlib (Hunter 2007), NumPy (van der Walt et al. 2011), SciPy (van der Walt et al. 2011), SExtractor (Bertin & Arnouts 1996), pyraf, TRIPPy (Fraser et al. 2016), emcee (Foreman-Mackey et al. 2013), IRAF (Tody 1986), and Gemini IRAF package, STSDAS.

ORCID iDs

Michaël Marsset  <https://orcid.org/0000-0001-8617-2425>
 Wesley C. Fraser  <https://orcid.org/0000-0001-6680-6558>
 Michele T. Bannister  <https://orcid.org/0000-0003-3257-4490>
 Megan E. Schwamb  <https://orcid.org/0000-0003-4365-1455>
 Rosemary E Pike  <https://orcid.org/0000-0003-4797-5262>
 Susan Benecchi  <https://orcid.org/0000-0001-8821-5927>
 J. J. Kavelaars  <https://orcid.org/0000-0001-7032-5255>
 Mike Alexandersen  <https://orcid.org/0000-0003-4143-8589>
 Ying-Tung Chen  <https://orcid.org/0000-0001-7244-6069>
 Brett J. Gladman  <https://orcid.org/0000-0002-0283-2260>
 Stephen D. J. Gwyn  <https://orcid.org/0000-0001-8221-8406>
 Jean-Marc Petit  <https://orcid.org/0000-0003-0407-2266>
 Kathryn Volk  <https://orcid.org/0000-0001-8736-236X>

References

Alvarez-Candal, A., Ayala-Loera, C., Gil-Hutton, R., et al. 2019, *MNRAS*, **488**, 3035
 Astropy Collaboration, Robitaille, T. P., Tollerud, E. J., et al. 2013, *A&A*, **558**, A33
 Bannister, M. T., Gladman, B. J., Kavelaars, J. J., et al. 2018, *ApJS*, **236**, 18
 Bannister, M. T., Kavelaars, J. J., Petit, J.-M., et al. 2016, *AJ*, **152**, 70
 Barucci, M. A., Alvarez-Candal, A., Merlin, F., et al. 2011, *Icar*, **214**, 297
 Benecchi, S. D., Noll, K. S., Grundy, W. M., et al. 2009, *Icar*, **200**, 292
 Bertin, E., & Arnouts, S. 1996, *A&AS*, **117**, 393
 Brown, M. E. 2001, *AJ*, **121**, 2804
 Christy, J. W., & Harrington, R. S. 1978, *AJ*, **83**, 1005

Foreman-Mackey, D., Farr, W., Sinha, M., et al. 2019, *JOSS*, **4**, 1864
 Foreman-Mackey, D., Hogg, D. W., Lang, D., & Goodman, J. 2013, *PASP*, **125**, 306
 Fraser, W., Alexandersen, M., Schwamb, M. E., et al. 2016, *AJ*, **151**, 158
 Fraser, W. C., Bannister, M. T., Pike, R. E., et al. 2017, *NatAs*, **1**, 0088
 Fraser, W. C., & Brown, M. E. 2012, *ApJ*, **749**, 33
 Fraser, W. C., Brown, M. E., & Glass, F. 2015, *ApJ*, **804**, 31
 Funato, Y., Makino, J., Hut, P., Kokubo, E., & Kinoshita, D. 2004, *Natur*, **427**, 518
 Gardner, J. P., Mather, J. C., Clampin, M., et al. 2006, *SSRv*, **123**, 485
 Gilmozzi, R., & Spyromilio, J. 2007, *Msngr*, **127**, 11
 Goldreich, P., Lithwick, Y., & Sari, R. 2002, *Natur*, **420**, 643
 Grundy, W. M., Noll, K. S., Roe, H. G., et al. 2019, *Icar*, **334**, 62
 Hodapp, K. W., Jensen, J. B., Irwin, E. M., et al. 2003, *PASP*, **115**, 1388
 Hook, I. M., Jørgensen, I., Allington-Smith, J. R., et al. 2004, *PASP*, **116**, 425
 Hunter, J. D. 2007, *CSE*, **9**, 90
 Johansen, A., Oishi, J. S., Mac Low, M.-M., et al. 2007, *Natur*, **448**, 1022
 Lacerda, P., Fornasier, S., Lellouch, E., et al. 2014, *ApJL*, **793**, L2
 Lim, P. L., Diaz, R. I., & Laidler, V. 2015, PySynphot User's Guide (Baltimore, MD: STScI), <https://pysynphot.readthedocs.io/en/latest/>
 Marsset, M., Fraser, W. C., Pike, R. E., et al. 2019, *AJ*, **157**, 94
 Nesvorný, D., Li, R., Youdin, A. N., Simon, J. B., & Grundy, W. M. 2019, *NatAs*, **3**, 808
 Nesvorný, D., & Vokrouhlický, D. 2019, *Icar*, **331**, 49
 Nesvorný, D., Youdin, A. N., & Richardson, D. C. 2010, *AJ*, **140**, 785
 Noll, K. S., Grundy, W. M., Stephens, D. C., Levison, H. F., & Kern, S. D. 2008, *Icar*, **194**, 758
 Ortiz, J. L., Thirouin, A., Campo Bagatin, A., et al. 2012, *MNRAS*, **419**, 2315
 Parker, A. H., & Kavelaars, J. J. 2010, *ApJL*, **722**, L204
 Peixinho, N., Delsanti, A., & Doressoundiram, A. 2015, *A&A*, **577**, A35
 Peixinho, N., Delsanti, A., Guilbert-Lepoutre, A., Gafeira, R., & Lacerda, P. 2012, *A&A*, **546**, A86
 Peixinho, N., Doressoundiram, A., Delsanti, A., et al. 2003, *A&A*, **410**, L29
 Pike, R. E., Fraser, W. C., Schwamb, M. E., et al. 2017, *AJ*, **154**, 101
 Pike, R. E., Kanwar, J., Alexandersen, M., Chen, Y.-T., & Schwamb, M. E. 2020, arXiv:2001.10144
 Robinson, J. E., Fraser, W. C., Fitzsimmons, A., & Lacerda, P. 2020, *A&A*, submitted
 Sanders, G. H. 2013, *JApA*, **34**, 81
 Schlichting, H. E., & Sari, R. 2008, *ApJ*, **673**, 1218
 Schwamb, M. E., Fraser, W. C., Bannister, M. T., et al. 2019, *ApJS*, **243**, 12
 Stern, S. A., Weaver, H. A., Spencer, J. R., et al. 2019, *Sci*, **364**, aaw9771
 Tegler, S. C., Bauer, J. M., Romanishin, W., & Peixinho, N. 2008, in *The Solar System Beyond Neptune*, ed. M. A. Barucci et al. (Tucson, AZ: Univ. Arizona Press), 105
 Tegler, S. C., & Romanishin, W. 1998, *Natur*, **392**, 49
 Tegler, S. C., & Romanishin, W. 2000, *Natur*, **407**, 979
 Tegler, S. C., & Romanishin, W. 2003, *Icar*, **161**, 181
 Tegler, S. C., Romanishin, W., & Consolmagno, G. J. 2003, *ApJL*, **599**, L49
 Tegler, S. C., Romanishin, W., & Consolmagno, G. J. 2016, *AJ*, **152**, 210
 Thirouin, A., & Sheppard, S. S. 2019, *AJ*, **158**, 53
 Tody, D. 1986, *Proc. SPIE*, **627**, 733
 van der Walt, S., Colbert, S. C., & Varoquaux, G. 2011, *CSE*, **13**, 22
 Wong, I., & Brown, M. E. 2017, *AJ*, **153**, 145